Direct Optical Lithography of Colloidal Metal Oxide Nanomaterials for Diffractive Optical Elements with 2π Phase Control

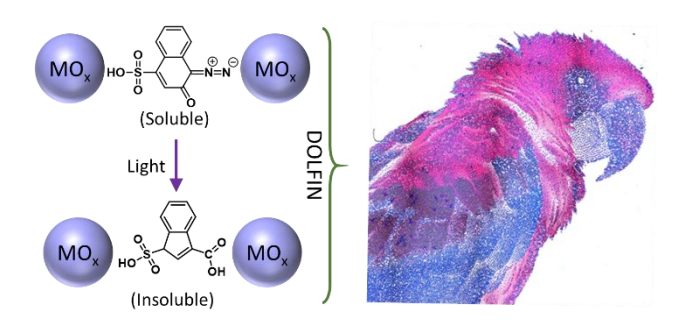
Jia-Ahn Pan[†], Zichao Rong[†], Yuanyuan Wang[†], Himchan Cho[†], Igor Coropceanu[†], Haoqi Wu[†], Dmitri V. Talapin^{*}, †, ‡

† Department of Chemistry, James Franck Institute, and Pritzker School of Molecular Engineering, University of Chicago, Chicago, Illinois 60637, United States

‡ Center for Nanoscale Materials, Argonne National Laboratory, Argonne, Illinois 60439, United States

Keywords: Direct optical lithography, patterning, nanoparticles, nanocrystals, sol-gel, oxides, diffractive optical elements, 2π phase shift

TOC graphic



Abstract

Spatially patterned dielectric materials are ubiquitous in electronic, photonic, and optoelectronic devices. These patterns are typically made by subtractive or additive approaches utilizing vapor-

phase reagents. On the other hand, recent advances in solution-phase synthesis of oxide nanomaterials have unlocked a materials library with greater compositional, microstructural, and interfacial tunability. However, methods to pattern and integrate these nanomaterials in real-world devices are less established. In this work, we directly optically pattern oxide nanoparticles (NPs) by mixing them with photosensitive diazo-2-naphthol-4-sulfonic acid and irradiating with widely available 405 nm light. We demonstrate the direct optical lithography of ZrO₂, TiO₂, HfO₂, and ITO NPs and investigate the chemical and physical changes responsible for this photoinduced decrease in solubility. For example, micron-thick layers of amorphous ZrO₂ NPs were patterned with micron resolution and shown to allow 2π phase control of visible light. We also show multilayer patterning and use it to fabricate features with different thicknesses and distinct structural colors. Upon annealing at 400 °C, the deposited structures have excellent optical transparency across a wide wavelength range $(0.3 - 10 \,\mu\text{m})$, a high refractive index $(n = 1.84 \,\text{at})$ 633 nm) and are optically smooth. We then fabricate diffractive optical elements, such as binary phase diffraction gratings, that show efficient diffractive behavior and good thermal stability. Different oxide NPs can also be mixed prior to patterning, providing a high level of material tunability. This work demonstrates a general patterning approach that harnesses the processability and diversity of colloidal oxide nanomaterials for use in photonic applications.

Introduction

Metal oxide layers are widely used as dielectric, semiconducting, or conductive layers in transistors, gas sensors, waveguides, diffractive optical elements, and recently, dielectric metasurfaces. Their widespread implementation can be attributed to thermal and mechanical robustness, coupled with desirable chemical, optical, and electronic properties such as optical transparency, high refractive index, and tunable conductivity. Importantly, high-resolution patterning is often essential to fully harness these properties and to integrate the oxide layers in practical devices.

An established method to fabricate oxide patterns involves photolithography of a sacrificial polymer resist layer followed by pattern transfer via etching (e.g., by reactive ion etching, RIE) or vapor-phase deposition (e.g., by atomic layer deposition, ALD) of the oxide layer. These methods work extremely well for some applications (e.g., in nanoelectronics) but face challenges when

applied to large-area substrates or thick oxide layers. Traditional ALD and RIE methods are also poorly applicable for low-cost applications (e.g., disposable radio-frequency identification tags and sensors). As an alternative, solution-based deposition techniques possess the advantages of lower costs, milder conditions, and shorter fabrication times. Various approaches have been developed to directly pattern solution-deposited oxide layers without the use of sacrificial photoresists. These include nano-imprint lithography,⁸ direct ink writing,⁹ dip-pen lithography,¹⁰ extreme-UV lithography¹¹, electron-beam lithography,¹² and direct optical lithography.⁷ Among these, direct optical lithography through a light-induced change in solubility of a photosensitive oxide ink is particularly attractive due to its simplicity, good resolution, and high throughput. This method can also utilize established light projection systems that have already been developed extensively for microelectronics, thus facilitating its facile and widespread implementation. Furthermore, developments in the chemistry of the photosensitive inks can be further adapted for light-based 3D printing technologies such as stereolithography and two-photon lithography.¹³⁻¹⁴

Among the different solution-processible precursors for inorganic materials, colloidal nanoparticles (NPs) allow for high atom economy during the precursor-to-inorganic layer transformations because they already contain multiatomic units of the target phase. This high atom economy translates into small volume contraction during annealing of patterned precursor layers. Colloidal oxide NPs are formed by controlled hydrolysis/condensation reactions in either aqueous or nonaqueous media. The aqueous route—commonly referred to as the sol-gel process—involves the hydrolysis and condensation of metal oxo complexes in either acidic or basic conditions. On the other hand, nonaqueous techniques initially developed for synthesizing luminescent quantum dots have been applied to making colloidal oxide NPs. This method involves the hot injection or heating up of metal oxide precursors in the presence of long chain ligands (e.g., oleic acid, oleylamine, trioctylphosphine oxide) in an organic solvent. With a large-scale industry developed around oxide NPs, a multitude of applications should benefit from the ability to directly optically pattern these NPs. 20

Oxide NPs can be photopatterned by embedding them in a matrix of photosensitive organic monomers subsequently polymerized by light.^{13, 21} A common issue with this approach is phase separation between the inorganic and organic components, which can affect properties like transparency and porosity.²² Alternatively, photosensitivity can be built into the NPs themselves by tailoring their ligand chemistry. Giannelis, Ober, and coworkers have systematically

investigated the use of oxide NPs (e.g., HfO₂, ZrO₂, ZnO) with short chain carboxylate ligands for high-resolution deep-UV and extreme-UV lithography.²³⁻²⁴ They proposed mechanisms involving photo-induced ligand desorption and ligand exchange leading to solubility changes. Other patterning methods such as crosslinking long-chain ligands,²⁵⁻²⁷ photocleavable ligands that change polarity upon decomposition,²⁸ and light sensitive DNA moieties²⁹ have been used to pattern metal or semiconductor NPs and should be extendable to oxide NPs as well.

In the last few years, we have been developing methods for the direct optical lithography of functional inorganic nanomaterials (DOLFIN), which emphasizes minimizing the amount of organic components in the patterned layers. $^{30-31}$ Although inorganic—organic hybrid materials are appropriate—even advantageous—for certain applications (e.g., flexible substrates and bio interfacing), there are many important applications that have been hindered by the inclusion of organic components. 32 These include applications that require strong electronic coupling between NPs, infrared transparency, high refractive indices, and wide thermal tolerance. One instance of these requirements is the fabrication of phase-shifting diffractive optical elements (DOEs), which utilize the principle of diffraction and interference to manipulate the properties of light. These transparent DOEs shape the wavefront of light by spatial variations in the retardation of incident light. To achieve arbitrary wavefront shaping, full 2π phase retardation is required, which can be achieved through patterns of sufficiently thick films with high refractive indices. Moreover, these optical devices often require good thermal and mechanical robustness for operational longevity, which may be compromised by the inclusion of a large organic fraction.

Herein, we use DOLFIN to fabricate high-performing oxide DOEs with full 2π phase control. Such optical elements have stringent requirements such as a large thickness, high refractive index, and optical-grade smoothness of patterned layers. A photosensitive oxide ink was formulated by mixing electrostatically stabilized oxide NPs with 1–25 wt % of the diazo compound 1-diazo-2-napthol-4-sulfonic acid (DNS), which is photosensitive to UV-blue light (350–450 nm). We directly photopattern thick (> 1 μ m) films of amorphous zirconia NPs, which allow for 2π phase control of visible light. These structures are highly transparent, have a high refractive index ($n \sim 1.84$), and can withstand multiple layer patterning. To demonstrate its optical capabilities, we fabricate films with structurally colored pixels as well as binary transmission gratings that show high diffraction efficiencies. We also show generalizability to various types of electrostatically stabilized oxide NPs (TiO₂, HfO₂, and ITO) made by different synthetic methods. This work

showcases the capability of direct patterning methods for colloidal nanomaterials and their use in photonic applications.

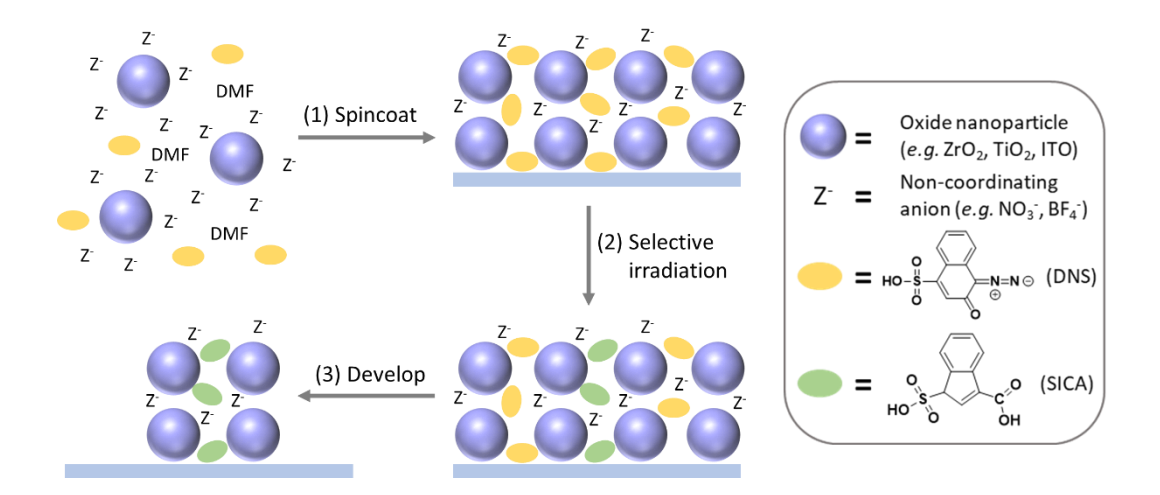
Results and Discussions

Selection of diazo-2-naphthol-4-sulfonic acid (DNS) as the photosensitive compound. To make optical elements with good diffractive capabilities, the patterning of thick oxide layers is required. This can be achieved by direct optical lithography of a thick film of oxide NPs mixed with a photosensitive additive, with the caveat that the oxide matrix needs to be highly transparent at the irradiation wavelength. This crucially allows the exposure light to penetrate deep into the film, decomposing the photosensitive compound throughout the thickness of the film. Since many oxide materials absorb in the UV, we decided to utilize a compound that is sensitive to violet (405 nm) light. One of the most well-known classes of commercial photoresists for UV-violet lithography are the diazonaphthoquinone (DNQ) photoresists, which consist of a photosensitive DNQ sulfonate ester mixed with a transparent phenolic polymer matrix.³³ Upon irradiation, the DNQ compound decomposes into a transparent indene carboxylic acid, changing the solubility of the resist in an aqueous base developer. Although cutting-edge photolithography has moved to deep-UV and extreme-UV exposure, the DNQ photoresists are still widely used in microlithography workflows.

Inspired by the commercial success of DNQ-polymer photoresists, we investigated the use of DNQ-like compounds to directly pattern thick layers of oxide NPs. We explored several DNQ variants including 4-(1-methyl-1-phenylethyl)phenyl 3-diazo-3,4-dihydro-4-oxo-1-naphthalenesulfonate (DNQ-Ar), 2-diazo-1-naphthol-4-sulfonic acid (2-DNS) and 1-diazo-2-naphthol-4-sulfonic acid (1-DNS). All these compounds decompose into 3-sulfo-3H-indene-1-carboxylic acid (SICA) upon photoirradiation. The chemical structures of these compounds are shown in **Table S1** and **Scheme 1**. We first tested the use of DNQ-Ar, a typical sulfonate ester variant used in commercial photoresists. Unfortunately, it did not significantly change the solubility of oxide NPs upon photoirradiation (i.e., low contrast), which we attribute to the interference of the phenol reaction products. On the other hand, DNQ variants with no phenol adducts (DNQ-Cl, 2-DNS, 1-DNS) were found to appreciably alter NP solubility after photoirradiation. However, we did not further investigate the

use of DNQ-Cl due to its highly reactive sulfonyl chloride moiety which is easily hydrolyzed, releasing H⁺ and Cl⁻ ions that can prematurely destabilize NPs by perturbing the pH or by binding to NP surfaces. ³⁴

Scheme 1. Direct photolithography process of oxide nanoparticles with DNS.



We obtained the best and most reproducible results with the sulfonic acid variants of DNQ, such as 1-DNS and 2-DNS. These two compounds are regioisomers (the diazo and oxo positions on the ring are swapped), but they both photodecompose into SICA due to an intermediate Wolff rearrangement step (**Scheme S1**). In this report, we primarily utilize 1-DNS as it is commercially available, but have found 2-DNS to perform equivalently. For simplicity, we will henceforth use DNS to refer to 1-DNS.

We first characterized the photochemical properties of DNS on its own before implementing it in a NP ink. **Figure 1A** shows the absorption spectra of DNS before and after its photodecomposition into ICA. DNS absorbs 405 nm light strongly with an absorption coefficient of $\epsilon_{405 \text{ nm}} = 4.23 \times 10^3 \text{ M}^{-1} \text{cm}^{-1}$. Upon photoirradiation, it decomposes into SICA, which has an absorption coefficient at 405 nm that is five orders of magnitude smaller ($\epsilon_{405 \text{ nm}} = 4.42 \times 10^{-2} \text{ M}^{-1} \text{cm}^{-1}$). This shows that the photodecomposition process is highly sensitive and efficient. The pronounced photobleaching of DNS also contributes to the ability of light to penetrate deep into a film, facilitating the pattering of thick NP layers.

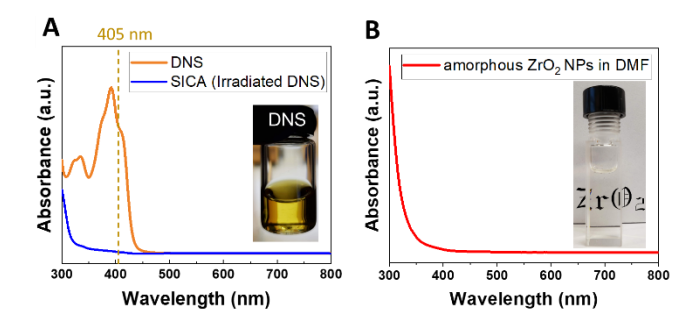


Figure 1. Absorption spectra of (A) diazo-2-naphthol-4-sulfonic acid (DNS) before and after its photodecomposition into 3-sulfo-3H-indene-1-carboxylic acid (SICA) and (B) amorphous ZrO₂ NPs after solvent exchange from water into DMF. Insets: photographs of the DNS and ZrO₂ NP solutions.

Photochemically active oxide NP inks. To prepare the photosensitive colloidal dispersion of NPs, both the DNS compound and the NPs must be highly soluble in a suitable solvent. *N*,*N*-dimethylformamide (DMF) was chosen as the solvent because it solubilizes both DNS and electrostatically charged NPs.³⁵ DMF also has an acceptably low boiling point (153 °C), which facilitates the spin coating of thick films.

Depending on the method of NP synthesis, different approaches were employed to obtain stable colloids of NPs in DMF (**Scheme S2**). NPs synthesized by aqueous sol–gel methods are already electrostatically stabilized and can be dispersed in DMF by a simple solvent exchange procedure from H₂O. We found that the complete removal of water was necessary due to the insolubility of DNS in water. However, since the dielectric constant of DMF is significantly lower than that of H₂O (36.7 versus 80.1), this procedure only works for reasonably small sized NPs (<20 nm) with highly noncoordinating anions (e.g., NO₃-). On the other hand, a different process is used for NPs capped with long chain organic ligands (e.g., oleic acid). For these NPs, a stripping agent (e.g., NOBF₄) is used to remove the organics and replace it with noncoordinating anions, rendering them soluble in DMF.³⁵

The photosensitive oxide NP ink is then obtained by simply adding DNS to the colloidal oxide NP solution in DMF. The percentage dry mass of DNS to NPs was optimized for each type

of NP, typically ranging between 1–25 wt %. In this report, we frequently utilize amorphous ZrO₂ NPs with positively charged surface and nitrate counterions as a convenient material system to demonstrate concepts applicable to a broad class of oxide NPs. After solvent exchange into DMF, these ZrO₂ NPs remain well-dispersed as indicated by their small hydrodynamic size (~6 nm) and large positive zeta potential (+45 mV) (**Figure S1**). The particles are stable to aggregation on the timescale of weeks. The colloidal solution is visibly clear without any cloudiness and is highly transparent to visible light, including 405 nm radiation (**Figure 1B**). The addition of DNS only slightly perturbs the NP colloidal stability by causing a small reduction in the zeta potential (+45 mV to +32 mV) upon the addition of an excess of DNS (100 wt % of DNS to NPs), which we attribute to the increase in ionic strength from the dissociation of DNS in DMF (**Figure S1b**). We thus infer that DNS only interacts weakly with the NC surface by contrasting this behavior with the drastic changes of zeta potential observed during the addition of strongly coordinating ionic ligands. ³⁶⁻³⁷ The highly charged NPs allow us to make highly concentrated amorphous ZrO₂ NP solutions (e.g., 250 mg/mL ZrO₂ NPs + 62.5 mg/mL DNS in DMF) that remained colloidally stable and transparent.

This method is generalizable to several other oxide NP solutions obtained by either the solvent exchange method (e.g., anatase TiO₂ NPs) or by the NOBF₄ ligand stripping method³⁵ (e.g., tetragonal phase ZrO₂ NPs, monoclinic HfO₂ NPs, and cubic phase ITO NPs), but with nuances in terms of the ultimate concentrations achievable and percentage of DNS required for patterning. For instance, NPs obtained from the ligand stripping method usually require less DNS for patterning (as low as 1 wt % of DNS to NPs). We attribute this to their better monodispersity and higher crystallinity, which lead to a smaller percolation threshold for 3D aggregation and a steeper van der Waals attractive potential, respectively.

Insights into the mechanism of patterning oxide NPs with DNS. The direct photopatterning process of oxide NPs with DNS is shown in **Scheme 1**. First, the ink is spincoated on a substrate to form a smooth layer of NPs (step 1). As the solvent evaporates, the DNS molecules begin to interact more with the charged NPs and condense around them. Even prior to its photodecomposition, the DNS molecules serve an important role as spacers for the NPs, preventing them from aggregating irreversibly due to van der Waals forces. Hence, without light exposure, we found that the NP–DNS films can be redissolved in DMF. In contrast, oxide NPs deposited

without DNS were found to be irreversibly insoluble in DMF upon drying. In this case, we hypothesize that NPs fall into the primary wells of their DLVO pair potentials, preventing any further manipulation of their solubilities.

Area-selective photoirradiation of the NP–DNS film leads to the decomposition of DNS into SICA in those regions (step 2 in **Scheme 1**). This is confirmed with Fourier transform infrared (FTIR) spectroscopy (**Figure S4**) by disappearance of the C=N=N and C−N≡N stretching peaks (2110 cm⁻¹ and 2164 cm⁻¹, respectively)³⁸ and the appearance of carboxylic acid peaks (1710 cm⁻¹, 1426 cm⁻¹). This is also corroborated by electrospray ionization mass spectroscopy (ESI-MS) in the negative ion mode (**Figure S5A**), which shows the molecular mass change from 2-DNS (m/z = 249) to SICA (m/z = 239). This photodecomposition significantly reduces the solubility of the film in the regions that were irradiated, while unexposed areas remain highly soluble in DMF (step 3 in Scheme 1). Hence, oxide NP patterns are revealed upon development with DMF.

To understand how the photoconversion of DNS to SICA decreases NP film solubility, we further investigated the chemical and physical changes that occur during this process. It is well-known that the photodecomposition of DNQ-4-sulfonate esters results in a significant increase in acidity.³³ In the case of DNS, ESI-MS measurements in the positive mode revealed a significant increase in the (DMF-H)⁺ to (DMF-Na)⁺ ratio after irradiation of 2-DNS (**Figure S5B**). Na⁺ ions leached from glassware and present in solvents are commonly detected in ESI-MS. This appreciable increase in the protonation of DMF means that the acidity of the solution has increased. In other words, SICA is a stronger Brønsted–Lowry acid than DNS, which allows it to protonate DMF. Based on the calculation of pK_a values using the ARChem SPARC software,³⁹⁻⁴⁰ we found that the increase in acidity can be attributed to the ring hydrogen in SICA, which has a significantly lower pK_a value than both sulfonic and carboxylic acid hydrogens (**Figure S6**).

Although our experimental and theoretical results support an increase in acidity upon photodecomposition of DNS into SICA, they do not prove that this acidity change is primarily responsible for the solubility change of the NPs. To probe this link, we carried out control experiments with two commercial photoacid generators (PAGs)—an ionic PAG and a nonionic PAG—that decompose under 365 nm light to produce strong acids (**Figure S7**). When either of these two PAGs were used in replacement of DNS (at the same molar concentration), areas of the film that were exposed to light increase in solubility, which is distinctively different than the behavior of NP–DNS films. Thus, we infer that although the DNS to SICA conversion increases

the acidity of the film, this effect is probably not the primary reason for the solubility reduction of the oxide NPs.

Another patterning mechanism which we considered involves the release of heat during the conversion of DNS into SICA. This conversion includes a highly exothermic Wolff rearrangement (-65 kcal/mol) that has been predicted to increase the local temperature up to 200 °C.⁴¹ Such highly localized hot spots could promote chemical reactions in the film, such as the condensation of surface hydroxyl groups into Zr-O-Zr interparticle bonds that reduce film solubility. To determine the importance of this effect, we carried out a control experiment by adding pre-irradiated DNS (i.e. SICA) to a solution of NPs (**Figure S12**). This resulted in an immediate gelation of the NP solution (**Figure S12b**), which means that the heat release is not essential for pattern formation. However, this heat release may affect the diffusion rate of SICA, which has implications for the line edge roughness and ultimate resolution of this patterning approach.

Finally, we considered the differences in the way DNS and SICA interacts with the NP surface. The decomposition of DNS into SICA involves a conversion of diazo and oxo groups into a carboxylic acid group, which has strong affinity to NP surfaces acting as an X-type ligand. This causes SICA to bind more strongly to NP surfaces, inhibiting the formation of electrostatic double-layer repulsive interactions upon reintroduction of the DMF solvent. This effect is supported by a significant decrease in the zeta potential of the NPs upon photoirradiation of DNS (**Figure S1b**). Furthermore, the presence of two potential binding sites (the sulfonic and carboxylic acid groups) in SICA allows it to serve as a crosslinker between two NPs, further cementing the NPs in place. As a control, we added an equimolar of benzene-1,4-dicarboxylic acid (BDA) to a solution of NPs and observed that the solution had a significantly higher viscosity than a DNS-NP solution, but did not gel like the SICA-NP solution (**Figure S12b**). Hence, our studies support a patterning mechanism involving the significant increase in binding and cross-linking ability when DNS photo-decomposes into SICA.

Direct optical lithography of oxide NPs with DNS. The direct patterning of oxide NPs with DNS was found to be generalizable across various types of NPs, provided that the NPs have good colloidal stability and form smooth films upon spincoating. **Figure 2** shows optical microscope images of direct optically patterned amorphous and tetragonal ZrO₂ NPs, anatase TiO₂ NPs,

monoclinic HfO₂, and cubic ITO NPs. All these patterns result from a pronounced decrease in NP solubility in regions that were exposed to 405 nm light.

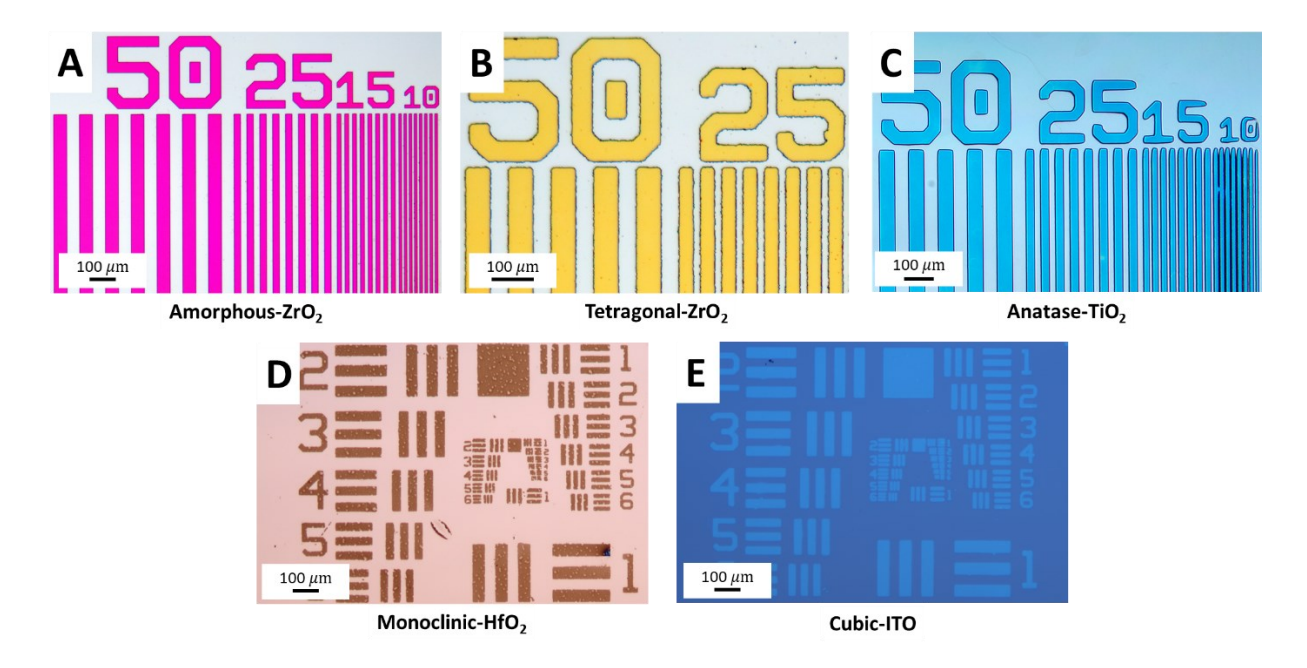


Figure 2. Optical microscope images of various oxide NPs optically patterned using DNS. (A) Amorphous ZrO₂ NPs, (B) tetragonal phase ZrO₂ NPs, (C) anatase TiO₂ NPs, (D) monoclinic HfO₂ NPs, and (E) cubic phase indium tin oxide NPs.

For more in-depth studies, we chose amorphous ZrO₂ NPs as our model system due to ease of processability and pattern robustness across a variety of parameters. The NPs can be patterned on glass or silicon wafers using a variety of exposure wavelengths (365 nm, 375 nm, 405 nm, and 450 nm) and exposure systems (LED light through a chrome mask, maskless laser writer, and LED display). We carried out resolution and thickness tests of the amorphous ZrO₂ NP patterns (**Figure 3**). The smallest pattern feature size was 1.2 μ m lines (**Figure 3A**), limited by the resolution of our direct laser writer. The exposure doses were comparable to those used for commercial DNQ resists, ⁴² with a 500 nm thick film of ZrO₂ NPs requiring a minimum dose of <100 mJ/cm².

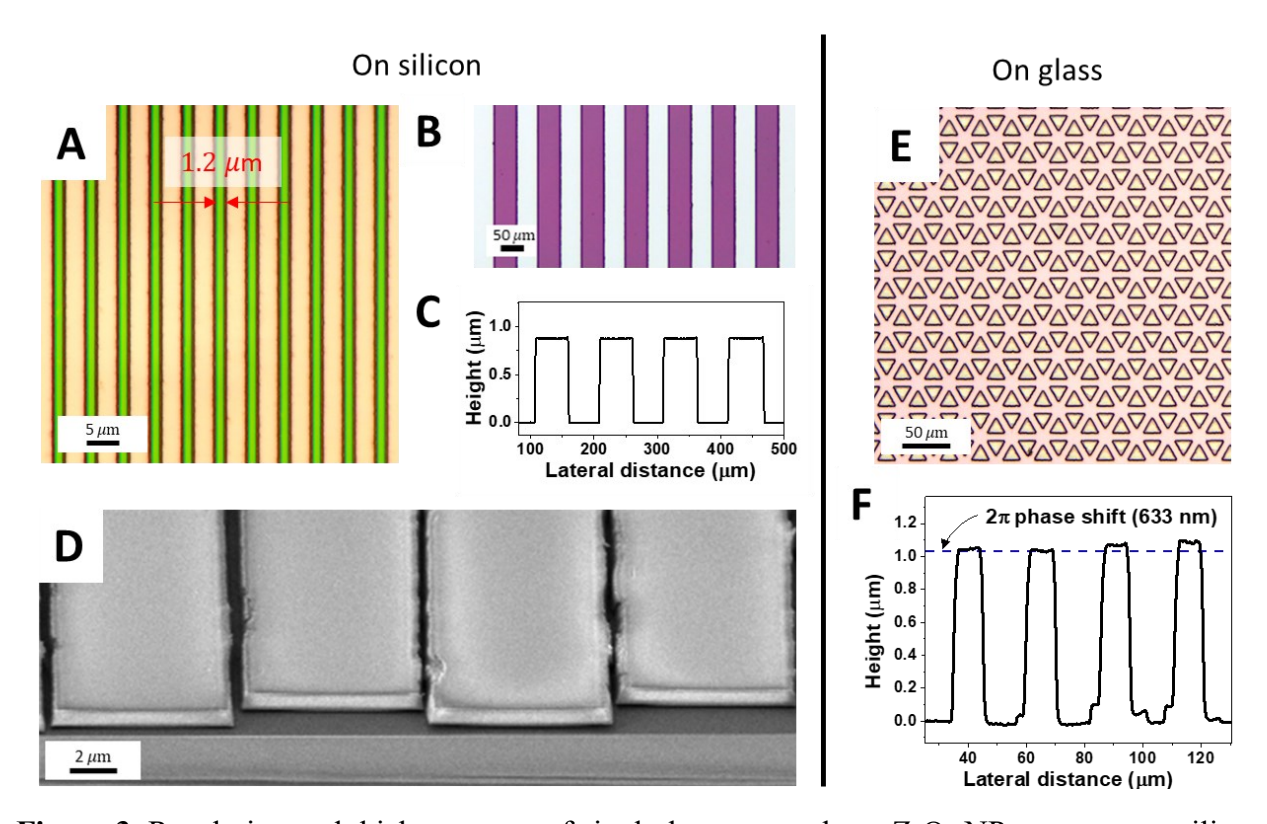


Figure 3. Resolution and thickness tests of single-layer amorphous ZrO_2 NPs patterns on silicon and glass substrates. Optical microscope images (A, B, E) and profilometer heights (C, F) of the patterns. The dotted line in (F) indicates the height required for a material with n = 1.61 to induce a 2π delay in the phase of 633 nm light. (D) Tilted SEM image of thick (overexposed) patterns.

With regards to thickness, we patterned structures that are sufficiently thick to allow for 2π phase delay of visible light. The thickness, t, required to shift the phase of incident light by 2π is given by $t = \lambda/(n-1)$, where n is the refractive index of the material and λ is the light wavelength in vacuum. With an ellipsometer, we determined the refractive index of an amorphous ZrO_2 film to be around n = 1.6 at $\lambda = 633$ nm, which gives a thickness requirement of about 1 μ m. With that in mind, we successfully deposited and patterned amorphous ZrO_2 NP layers that were routinely thicker than 800 nm and even beyond 1 μ m (**Figure 3B,C,F**). The patterns on glass surpass the requirement for 2π phase control in the visible (dotted line in **Figure 3F**), demonstrating the viability of this approach for the fabrication of diffractive optical elements with full control over the phase of light.

The deposition of thick NP layers in a single step is often found to be challenging due to internal stresses during film drying which leads to cracking.⁴⁴ Still, there have been reports showing the deposition of smooth NP films that are several micrometers thick.⁴⁵ To prepare patterns of thick NP films, we optimized both the NP solution processing and the deposition parameters. One straightforward way to increase film thickness is by increasing NP concentration. However, this needs to be done while maintaining good colloidal stability. We found that higher NP concentrations were attainable by introducing a hexane washing step before the final dispersion of NPs in DMF. This additional washing step extracts the residual toluene that was previously added as a nonsolvent to precipitate the NPs. Since hexane is immiscible with DMF and the NPs, it simply evaporates away after the final dissolution of NPs in DMF. This allows significantly higher NP concentrations to be formulated. Also, we found that infrared heating during spincoating helped in the formation of smooth and thick NP films. Besides increasing the solvent evaporation rate, the increased temperature may also relax the internal stresses in the film, reducing its susceptibility to cracking.

We also evaluated the capability of our approach for multilayer patterning (**Figure 4**). The process of deposition, irradiation, and development can be done repeatedly on the same substrate in a layer-by-layer fashion (**Figure 4A**). Using inks with different NP concentrations for each layer, oxide patterns of varying heights should be attainable. Layers can even be deposited on top of each other, allowing a total of $(2^n - 1)$ height variations to be obtained after n number of patterned layers. As proof of this concept, we patterned a multicolored parrot image by depositing pixels of three different heights with only two deposition steps (**Figure 4B–D**). The height of each pixel was chosen such that thin-film interference produced the desired color (magenta ~ 420 nm, green ~ 350 nm, and blue ~ 70 nm, measured by profilometry). This should be extendable to many more layers, allowing it to be used for devices with variations in topography, such as blazed diffraction gratings or colored printing.

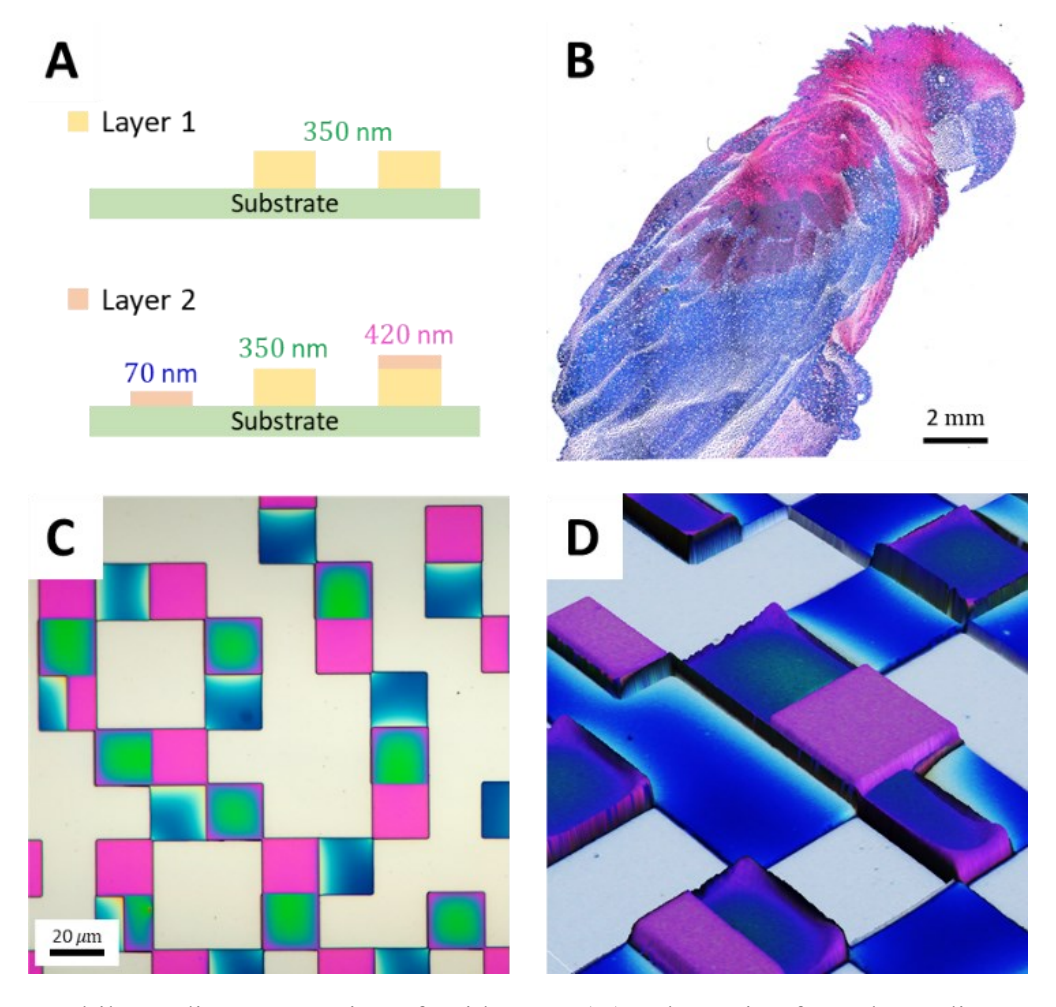


Figure 4. Multilayer direct patterning of oxide NPs. (A) Schematic of two-layer direct patterning process to obtain pixels with three different heights. (B–D) Fabrication of a colored parrot image by patterning two layers of amorphous ZrO₂ NPs. Low-magnification (B) and high-magnification (C) optical microscope images. (D) Three-dimensional height profile from a confocal optical microscope.

Characterization of amorphous ZrO₂ NP–SICA films. We evaluated the chemical, thermal and optical properties of ZrO₂ NP–SICA films. After deposition and irradiation with 405 nm light, the films have good transparency in the visible and near-IR regions (**Figure 5A**, red). However, there are strong mid-IR absorbing peaks due to SICA (1710 cm⁻¹, 1426 cm⁻¹) and Zr–OH (3370 cm⁻¹, 1370 cm⁻¹), which remain even after DMF development (**Figure 5B**, red and **S4**). Annealing at 400 °C decomposes most of the SICA from the film and condenses the Zr–OH groups into new Zr–O–Zr bonds (500–1000 cm⁻¹, broad). Nevertheless, annealing is insufficient to induce

crystallization of the ZrO₂ as indicated by purely amorphous powder X-ray diffraction (XRD) peaks (**Figure S8**).

The result of the thermal treatment is an oxide layer that is highly transparent across a broad range of wavelengths, from 300 nm to 10 μ m (**Figure 5A,B**, blue). The oscillations in the transmittance spectrum of the annealed film (e.g., the dips around 300 nm and 750 nm) can be attributed to thin-film interference effects, which is supported by good agreement of the measured transmission data with optical modeling using the transfer matrix method (**Figure S9**).

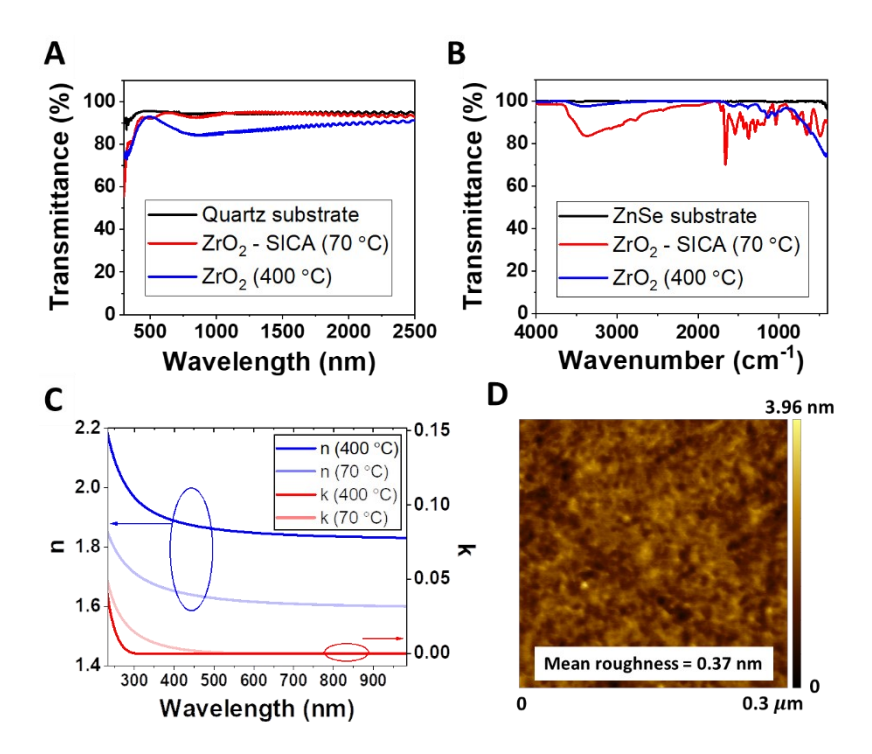


Figure 5. Optical and surface roughness characterization of amorphous ZrO₂ NP–SICA films. Film transmission spectra in the visible and near-IR regions (A) and in the mid-IR region (B). (C) Real and imaginary parts of the refractive index obtained by fitting spectroscopic ellipsometry data to a Tauc–Lorentz model. (D) Atomic force microscopy image after annealing the film at 400 °C.

The optical n and k constants of ZrO_2 NP films before and after annealing were obtained by spectroscopic ellipsometry, with the oxide layer modeled by the Tauc-Lorentz dispersion formula showing good fits with low χ^2 values between the model and experimental data (**Figure 5C and**

S10). The results show that annealing at 400 °C increases the refractive index of the film by about $\Delta n = 0.2$ throughout the visible region. The refractive index of the annealed ZrO₂ layer is still lower than that of ZrO₂ deposited by atomic layer deposition (n = 1.84 vs. n = 2.1 @ 633 nm), ⁴⁶ which shows that the NP film is not fully densified. This is common for solution-deposited oxides, but methods such as high-pressure annealing can be used to achieve full densification. ⁴⁷ We also measured the mean surface roughness of the annealed ZrO₂ film to be 0.37 nm by atomic force microscopy (AFM) (**Figure 5D**). This should allow for minimal scattering loses, which further reinforces the suitability of our patterned films for high-efficiency optical applications.

Fabrication and testing of oxide NP gratings. As a proof-of-concept, we fabricated and tested diffractive optical elements (DOEs) made with patterned ZrO₂ NPs. DOEs are optical devices that spatially shape the wavefront of propagating light. One of the simplest DOEs is the one-dimensional diffraction grating, which consists of a periodic pattern of stripes that either block light (amplitude gratings) or retard its phase (phase gratings). These changes lead to constructive and destructive interference in the far-field and the formation of bright spots on a screen (Figure 6A). Phase gratings are attractive due to their higher diffraction efficiencies, η_n , defined as the ratio of the power channeled into the n-th order diffraction peak to the incident light power. Without considering Fresnel reflections, an ideal binary (two-level) phase grating can channel 40.5% of the incident power into each of the ± 1 diffraction order. This is achieved when the grating has exactly equal stripe and spacing widths, with each stripe retarding the phase of light by exactly π .

We patterned ZrO₂ NPs stripes with 25 μ m line and spacing widths on a glass cover slip (**Figure 6B**). Upon illumination with a red laser light ($\lambda = 650$ nm), a diffraction pattern with many visible diffraction orders was produced (**Figure 6C**). To obtain quantitative diffraction efficiencies, we measured the zeroth and first order spots with a silicon detector and found that the +1 and -1 orders contain 37% and 32% of the incident light power respectively (the difference can be attributed to a small, nonzero angle of incidence), while the zeroth order spot contained less than 2% of the incident power (**Figure 6D**). These metrics are significantly better than that of a chromium amplitude mask (9% efficiencies for +1 and -1 diffraction orders) and should be improvable with further finetuning of the film thickness.

We also carried out thermal stability and laser tolerance tests on a ZrO₂ NP grating and compared its behavior to a commercial polymer grating (**Figure 6E**). The ZrO₂ NP grating was found to have good thermal stability up to the highest tested temperature of 500 °C, as shown by good optical transparency and clear diffraction patterns. It also was not visibly damaged upon irradiation upon a 5 s exposure to the second harmonic generation of a pulsed Nd:YAG laser at its maximum power. In contrast, the polymer grating began to warp around 150 °C and was completely unusable beyond 300 °C. It also visibly blackened upon exposure to the Nd:YAG laser. Thus, these ZrO₂ NP DOEs have good tolerance to high temperatures and high-powered lasers, which make them an appealing choice for applications that require such tolerance (e.g., gratings for distributed feedback lasers).

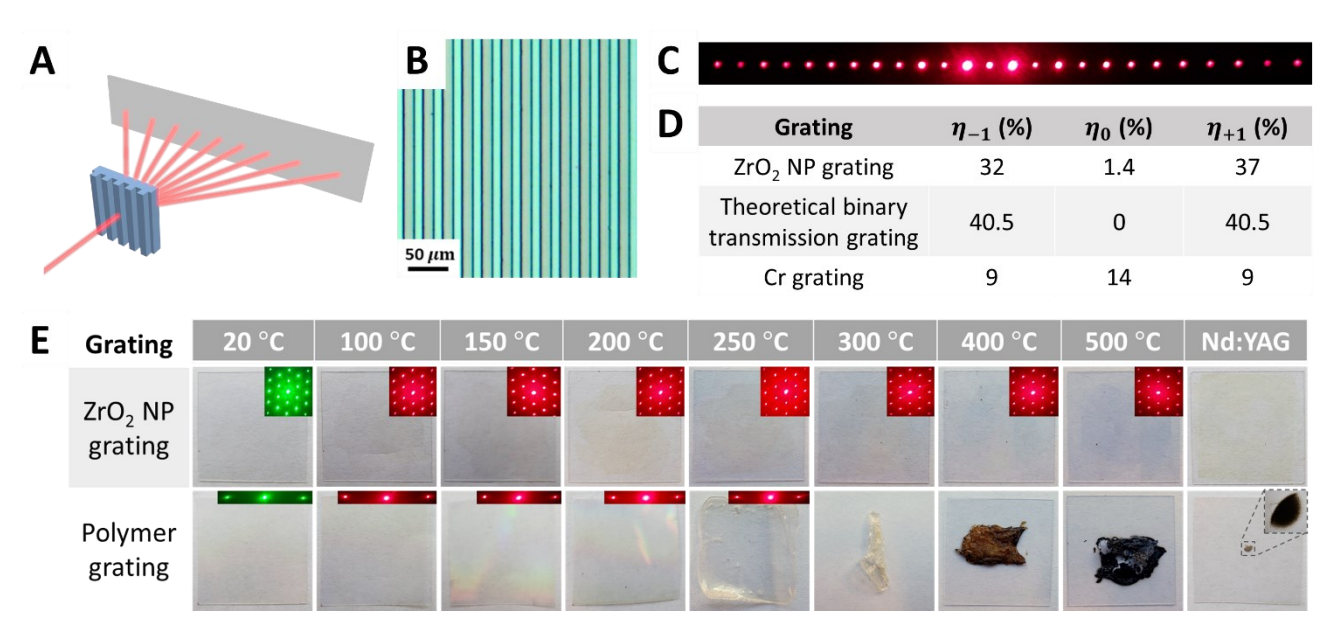


Figure 6. Characterization of diffraction gratings made by patterning amorphous ZrO₂ NPs. (A) Schematic showing the diffraction of a laser beam through a one-dimensional (1D) grating. Optical microscope image of a 1D ZrO₂ NP grating (B) along with its diffraction pattern (C) and grating efficiencies (D). The efficiencies of an ideal binary phase grating (theoretical) and a chromium grating are shown for comparison. (E) Thermal stability and laser tolerance of a ZrO₂ NP grating compared to a polymer grating. Thermal stability tests involved 10 minutes of heating on a hot plate, while the laser test involved a 5 second exposure to the second harmonic generation (532 nm) of a pulsed Nd:YAG laser (10 Hz, ~25 mJ/pulse). Insets: Diffraction patterns produced by the gratings.

The direct photopatterning of oxide NPs should also find utility in many other applications besides the fabrication of DOEs. The facile patterning of ITO NPs will facilitate their usage as transparent conducting electrodes in optoelectronic devices. Recent advances have shown that the conductivity of solution-deposited ITO can approach that of films deposited by vapor deposition techniques. Application deposited ITO NPs with their optical properties tunable by NP size and doping concentration are actively investigated for applications using localized surface plasmon resonance (LSPR). Similarly, the ability to pattern TiO₂ NPs can have implications for photovoltaic, photocatalytic, and electrochromic applications by allowing the deposition of optimal patterns that allow for better performance and interfacing. S3-54

Tunability and miscibility of oxide NPs for compositional and microstructural control. A significant advantage in utilizing solution-phase NPs is the access to a large library of NPs with various optical, electrical, chemical, and thermal properties. Even NPs with the same chemical composition can have nuances in terms of their crystal phase, shape, and surface chemistries which influence their properties. For instance, highly crystalline NPs are already highly compacted, and their atoms do not significantly rearrange or further densify upon annealing. Thus, we found that patterns of tetragonal ZrO2 NPs undergo no measurable shrinkage upon annealing at 390 °C (Figure 7A). During this process, the refractive index of the film does not significantly change $(n \sim 1.73 \ @ 633 \ nm)$. Assuming the refractive index of ZrO₂ NPs is n = 2.15 and the gaps between them is air (n = 1), this gives a solid fraction of $\phi_{ZrO_2} = 0.65$ by the symmetric Bruggeman effective medium approximation (or $\phi_{\rm ZrO_2} = 0.63$ by the volume-weighted index method),⁵⁵ which is close to the expected volume fraction of random closely packed spheres. In contrast, amorphous ZrO₂ NP patterns shrank by about 33% upon annealing at 400 °C (Figure **7B**), along with a refractive index increase from n = 1.61 to n = 1.84 at 633 nm, as discussed previously. This increased refractive index can be attributed to rearrangement and condensation of Zr and O atoms, which allows the gaps between NPs to be filled. Besides differences in the crystal phases, various NP shapes can also be explored in the future, such as mesoporous ZrO₂ nanoframes.56

Further tuning of the patterned oxide layers can be done using mixtures of NPs. This modular, "mix-and-match" approach can be used to synergistically combine the properties of two or more NPs in a way that leads to better performance than each individual component. To illustrate this concept, we patterned a mixture of amorphous ZrO2 NPs and tetragonal phase ZrO2 NPs (Figure 7C). We found that after annealing at 450 °C, layers containing a mixture of these two NPs have a higher refractive index (n = 1.88) compared to layers of tetragonal ZrO₂ NPs (n = 1.73) and amorphous ZrO₂ NPs (n = 1.84) on their own (Figure 7D). We hypothesize that this is due to the amorphous ZrO₂ filling in the gaps between the crystalline ZrO₂, forming what is commonly referred to as a "glass-ceramic". 57-58 Traditional approaches for the fabrication of glass-ceramic composites typically rely upon carefully controlled nucleation of crystals in a glassy matrix at high temperatures (often >1500 °C).⁵⁸ In contrast, our method allows for each oxide component to be synthesized separately, mixed together in desired ratios and finally patterned directly under mild conditions. Thus, our approach utilizes the versatility and convenience of colloidal NPs in the facile fabrication of increasingly sophisticated metal oxide patterns. It is also worth mentioning that multiple components can be reliably co-integrated within individual NPs, e.g., in from of coreshell or dumbbell nano-heterostructures. 59-60

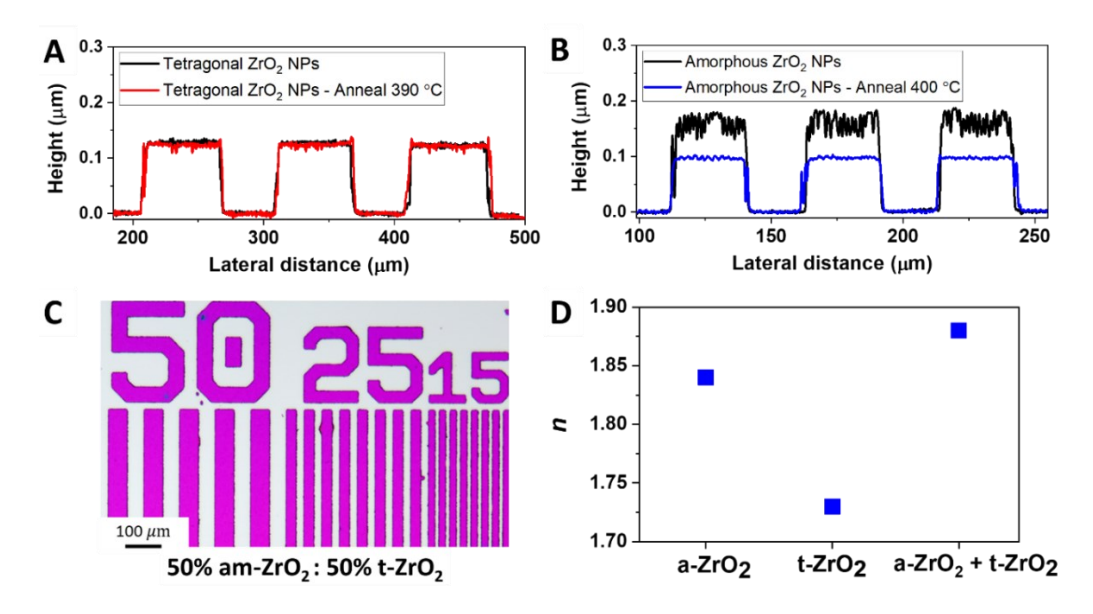


Figure 7. Profilometer heights of patterned tetragonal phase ZrO_2 NPs (A) and amorphous ZrO_2 NPs (B) before and after annealing. (C) Patterns of a 50:50 mixture of amorphous ZrO_2 NPs and tetragonal ZrO_2 NPs. (D) Refractive indices, n, of films made from amorphous ZrO_2 NPs,

tetragonal phase ZrO₂ NPs, and a 40:60 mixture of amorphous and tetragonal phase ZrO₂ NPs (all annealed at 450 °C).

Conclusions

In summary, we developed a general approach for direct optical patterning of metal oxide NPs that is polymer-free and uses minimal organics, thus circumventing the limitations of inorganic-organic hybrid patterning methods. The photosensitive oxide inks were formulated by mixing various electrostatically stabilized oxide NPs with the photosensitive 1-diazo-2-naphthol-4-sulfonic acid in DMF. Thick layers (>1 μ m) of amorphous ZrO₂ NPs can be patterned, allowing for 2π phase control of visible light. The oxide films have a high refractive index, good transparency across a wide wavelength range (300 nm - 10 μ m), and low mean surface roughness. Multilayer patterning was also shown through the fabrication of a structurally colored parrot image by depositing pixels of different thickness. We then used this patterning platform to make efficient diffractive optical elements (e.g., diffractive gratings) that are thermally and optically robust. Finally, we demonstrated the ability to pattern mixtures of NPs, which allow for increased compositional variability and complexity.

Experimental Section

Sources/syntheses of oxide nanoparticles. Amorphous ZrO₂ NPs with nitrate counterions (Zr10/15) were obtained as aqueous dispersions from Nyacol Nano Technologies, Inc. Titanium oxide NPs (Anatase, 15 wt %, 30 nm) were obtained from Nanostructured and Amorphous Materials, Inc.

Tin-doped indium oxide NPs capped with oleic acid/oleylamine were synthesized using a procedure by Lounis *et al.*⁶¹ Briefly, In(acetate)₃ (1.02 mmol), Sn(ethylhexanoate)₂ (0.18 mmol), octanoic acid (3.6 mmol), and oleylamine (10 mmol) were mixed with 10 mL of octyl ether and degassed at 80 °C for 30 minutes. The temperature was then increased to 150 °C under N₂ and held there for 1 hour. The temperature was then further increased to 280 °C and held there for another 2 hours. The NCs were purified several times by ethanol and toluene.

Tetragonal zirconia NPs capped with TOPO were synthesized by a procedure by Joo *et al.*¹⁸ Briefly, trioctylphosphine oxide (30 g) was degassed at 80 °C for 1 hour in a 3-neck round-bottom flask. The flask was sealed, brought into a glove box and Zr(O-iPr)₄·(IPA) (2.34 g, 6 mmol) and ZrCl₄ (1.75 g, 7.5 mmol) was added. The mixture was then degassed again at 70 °C for 30 mins. Under nitrogen, the solution was heated to 340 °C and held there for 2 hours. The NCs were purified several times by acetone and toluene.

Monoclinic HfO₂ NPs capped with TOPO were synthesized by a procedure by Tirosh et al.⁶² Briefly, trioctylphosphine oxide (30 g) was degassed at 80 °C for 1 hour in a 3-neck round-bottom flask. The flask was sealed, brought into a glove box and Hf(O-iPr)₄·(IPA) (2.85 g. 6 mmol) and HfCl₄ (1.95 g, 6 mmol) was added. The mixture was then degassed again at 70 °C for 30 mins. Under nitrogen, the solution was heated to 360 °C and held there for 2 hours. The NCs were purified several times by acetone and toluene.

Powder XRD data of all synthesized NPs are shown in Figure S11.

Preparation of NP-DNS ink

Nanoparticles in aqueous solution. For NPs colloidally stabilized by electrostatic interactions in water, a solvent exchange procedure to disperse NPs in DMF was developed. Using amorphous ZrO₂ NPs from Nyacol Nanotechnologies, Inc as an example, acetone (41 mL) was added to precipitate the ZrO₂ NP solution (13.4 wt %, 4 mL). The suspension was centrifuged and the pellet redispersed in DMF (8 mL), which was left to equilibrate overnight. The NPs were precipitated with the addition of toluene (17 mL) followed by centrifugation. The pellet was washed with hexane (15 mL) to remove residue toluene and then centrifuged. Finally, the pellet was dissolved in DMF at the desired concentration (>300 mg/mL achievable), with the help of vortexing, sonication and stirring. The NP solution was aged overnight before subsequent steps.

Organic-capped nanoparticles in nonpolar solvents. Organic-capped NPs were stripped of their native ligands by a modified NOBF₄ stripping method, by adding NOBF₄ in DMF (0.1 mL, ~20 mg/mL) to NP solution (1 mL, ~10 mg/mL). Flocculation of NPs was observed within a few seconds. The suspension was then vortexed and centrifuged. The supernatant was discarded and the pellet redispersed in DMF (0.1 mL), forming a clear solution. Toluene (1 mL) was added to

precipitate NPs and the suspension was centrifuged. The redispersion, precipitation and centrifugation were repeated one more time. The pellet was vortexed with hexane (1 mL) to extract residual toluene and the formed suspension was centrifuged. Finally, the pellet was dispersed in DMF at the desired concentration (>100 mg/mL typically achievable).

Mixing nanoparticles with DNS. To obtain the photosensitive oxide ink, DNS was mixed (either directly as a solid or predissolved in DMF) with NP solution in DMF. The NP concentration was first determined by measuring the residue solid weight after drying about 100 μ L of solution in a vacuum oven at 60 °C overnight. An amount of DNS between 1 and 25 wt % relative to the dried NP weight was used depending on the type of NPs. The mixture needs to be aged for several hours to work properly in subsequent steps.

Direct photolithography using nanoparticle-DNS ink

Silicon substrates and glass cover slips were first cleaned by sonication in acetone (10 mins) and then in IPA (10 mins). They were then treated with O₂ plasma (> 10 mins) immediately prior to usage. The nanoparticle-DNS ink was then spincoated on a substrate with a rotation speed between 300 and 8,000 rpm. Then, selective-area light exposure was carried out by one of two methods: (1) a home-made contact lithography setup which involves clamping the substrate with a chrome mask using two binder clips and exposing with an LED light source (M405LP-C1-405 nm, Thorlabs, measured power density ~30 mJ/cm²) or (2) a maskless direct-write laser system (MLA150, 405/375 nm, Heidelberg Instruments) in a cleanroom. After exposure, the patterns were developed by immersing the substrate into the DMF developer solvent, rinsed with IPA, and blow dried with a N₂ gun.

For multilayer patterning, the above procedure was followed by a brief annealing step (e.g., 70 °C, 2 mins), followed by an O₂ plasma treatment before the next deposition step. For samples that required precise alignment between the first and second pattern steps, five crosshair alignment marks were patterned in the first step and used for the alignment during the second step using the MLA150 software.

There are several modifications of this procedure depending on the NPs used. For amorphous ZrO₂ NPs, a postexposure bake step (70 °C, 30s) is necessary, particularly for thick films. In some

cases, immersing the substrate into a 2-methoxyethanol, 2-ME (for ~10 s) prior to DMF

development helps to reduce cracking of the patterned film.

Associated Content

Supporting Information. The supporting information is available free of charge at

http://pubs.acs.org.

Experimental details, characterization techniques, relevant chemical structures, mechanism

of DNS conversion to SICA, schematic of methods to obtain NPs in DMF, dynamic light scattering

and zeta-potential measurements, plots of van der Waals interaction energies between spheres of

different sizes, ³¹P-NMR spectra of TOPO-capped HfO₂ and ZrO₂ NPs including the effects of the

stripping procedures, additional FTIR spectra, ESI-MS data, results of pK_a calculation with the

SPARC calculator, pattern evaluation with other photoacid generators, modeling the film

transmittance with the transfer-matrix method, XRD spectra, spectroscopic ellipsometry fits with

the Tauc-Lorentz model, control mechanism studies with pre-irradiated DNS and BDA

Author information

Corresponding author

* E-mail: dvtalapin@uchicago.edu

Present addresses:

° Present address: State Key Laboratory of Coordination Chemistry, School of Chemistry and

Chemical Engineering, Nanjing University, Nanjing, 210023, China

Notes

The authors declare no competing financial interests.

Acknowledgements

We would like to thank T. Shpigel for reading the manuscript. This work was supported by the

Department of Defense (DOD) Air Force Office of Scientific Research under grant number

FA9550-18-1-0099 and by NSF under award number CHE-1905290. D.V.T. acknowledges

23

support from the Samsung Global Research Outreach Program on New Materials. This work was partially supported by the University of Chicago Materials Research Science and Engineering Center, which is funded by the National Science Foundation under award number DMR-2011854. Use of the Center for Nanoscale Materials, an Office of Science User Facilities operated for the U.S. Department of Energy (DOE) Office of Science by Argonne National Laboratory, was supported by the U.S. DOE under Contract No. DE-AC02-06CH11357. This work made use of the Pritzker Nanofabrication Facility, which receives partial support from the SHyNE Resource, a node of the National Science Foundation's National Nanotechnology Coordinated Infrastructure (NSF ECCS-2025633)."

References

- 1. Fortunato, E.; Barquinha, P.; Martins, R., Oxide semiconductor thin-film transistors: a review of recent advances. *Adv. Mater.* **2012**, *24* (22), 2945-2986.
- 2. Dai, J.; Ogbeide, O.; Macadam, N.; Sun, Q.; Yu, W.; Li, Y.; Su, B.-L.; Hasan, T.; Huang, X.; Huang, W., Printed gas sensors. *Chem. Soc. Rev.* **2020**, *49* (6), 1756-1789.
- 3. Kip, D., Photorefractive waveguides in oxide crystals: fabrication, properties, and applications. *Appl. Phys. B* **1998**, *67* (2), 131-150.
- 4. Yamada, I.; Ikeda, Y., Sol-gel zirconia diffraction grating using a soft imprinting process. *Appl. Opt.* **2017**, *56* (17), 5054-5059.
- Devlin, R. C.; Khorasaninejad, M.; Chen, W. T.; Oh, J.; Capasso, F., Broadband high-efficiency dielectric metasurfaces for the visible spectrum. *Proc. Natl. Acad. Sci. U. S. A.* 2016, 113 (38), 10473-10478.
- 6. Park, J.-S.; Zhang, S.; She, A.; Chen, W. T.; Lin, P.; Yousef, K. M. A.; Cheng, J.-X.; Capasso, F., All-Glass, Large Metalens at Visible Wavelength Using Deep-Ultraviolet Projection Lithography. *Nano Lett.* **2019**, *19* (12), 8673-8682.
- 7. Yeh, C. C.; Zan, H. W.; Soppera, O., Solution-Based Micro- and Nanoscale Metal Oxide Structures Formed by Direct Patterning for Electro-Optical Applications. *Adv. Mater.* **2018**, *30* (50), 1800923.
- 8. Kothari, R.; Beaulieu, M. R.; Hendricks, N. R.; Li, S.; Watkins, J. J., Direct Patterning of Robust One-Dimensional, Two-Dimensional, and Three-Dimensional Crystalline Metal Oxide Nanostructures Using Imprint Lithography and Nanoparticle Dispersion Inks. *Chem. Mater.* **2017**, *29* (9), 3908-3918.
- 9. Duoss, E. B.; Twardowski, M.; Lewis, J. A., Sol-Gel Inks for Direct-Write Assembly of Functional Oxides. *Adv. Mater.* **2007**, *19* (21), 3485-3489.
- 10. Su, M.; Liu, X.; Li, S.-Y.; Dravid, V. P.; Mirkin, C. A., Moving beyond Molecules: Patterning Solid-State Features via Dip-Pen Nanolithography with Sol-Based Inks. *J. Am. Chem. Soc.* **2002**, *124* (8), 1560-1561.
- 11. Jiang, J.; Chakrabarty, S.; Yu, M.; Ober, C. K., Metal oxide nanoparticle photoresists for EUV patterning. *J. Photopolym. Sci. Technol.* **2014**, *27* (5), 663-666.
- 12. Saifullah, M.; Subramanian, K.; Tapley, E.; Kang, D.-J.; Welland, M.; Butler, M., Sub-10 nm electron beam nanolithography using spin-coatable TiO2 resists. *Nano Lett.* **2003**, *3* (11), 1587-1591.

- 13. Kotz, F.; Arnold, K.; Bauer, W.; Schild, D.; Keller, N.; Sachsenheimer, K.; Nargang, T. M.; Richter, C.; Helmer, D.; Rapp, B. E., Three-dimensional printing of transparent fused silica glass. *Nature* **2017**, *544* (7650), 337.
- 14. Yee, D. W.; Lifson, M. L.; Edwards, B. W.; Greer, J. R., Additive Manufacturing of 3D-Architected Multifunctional Metal Oxides. *Adv. Mater.* **2019**, *31* (33), 1901345.
- 15. Jiang, C.; Lee, J.-S.; Talapin, D. V., Soluble Precursors for CuInSe2, CuIn1-xGaxSe2, and Cu2ZnSn(S,Se)4 Based on Colloidal Nanocrystals and Molecular Metal Chalcogenide Surface Ligands. *J. Am. Chem. Soc.* **2012**, *134* (11), 5010-5013.
- 16. Hench, L. L.; West, J. K., The sol-gel process. Chem. Rev. 1990, 90 (1), 33-72.
- 17. Park, J.; Joo, J.; Kwon, S. G.; Jang, Y.; Hyeon, T., Synthesis of Monodisperse Spherical Nanocrystals. *Angew. Chem. Int. Ed.* **2007**, *46* (25), 4630-4660.
- 18. Joo, J.; Yu, T.; Kim, Y. W.; Park, H. M.; Wu, F.; Zhang, J. Z.; Hyeon, T., Multigram scale synthesis and characterization of monodisperse tetragonal zirconia nanocrystals. *J. Am. Chem. Soc.* **2003**, *125* (21), 6553-6557.
- 19. Kanehara, M.; Koike, H.; Yoshinaga, T.; Teranishi, T., Indium Tin Oxide Nanoparticles with Compositionally Tunable Surface Plasmon Resonance Frequencies in the Near-IR Region. *J. Am. Chem. Soc.* **2009**, *131* (49), 17736-17737.
- 20. Rodríguez, J. A.; Fernández-García, M., *Synthesis, properties, and applications of oxide nanomaterials*. John Wiley & Sons: 2007; p 379-713
- 21. Liu, J.-g.; Nakamura, Y.; Ogura, T.; Shibasaki, Y.; Ando, S.; Ueda, M., Optically transparent sulfur-containing polyimide—TiO2 nanocomposite films with high refractive index and negative pattern formation from poly (amic acid)—TiO2 nanocomposite film. *Chem. Mater.* **2007**, *20* (1), 273-281.
- 22. Loste, J.; Lopez-Cuesta, J.-M.; Billon, L.; Garay, H.; Save, M., Transparent polymer nanocomposites: An overview on their synthesis and advanced properties. *Prog. Polym. Sci.* **2019**, *89*, 133-158.
- 23. Trikeriotis, M.; Bae, W. J.; Schwartz, E.; Krysak, M.; Lafferty, N.; Xie, P.; Smith, B.; Zimmerman, P.; Ober, C.; Giannelis, E., *Development of an inorganic photoresist for DUV, EUV, and electron beam imaging.* SPIE: 2010; Vol. 7639.
- 24. Li, L.; Liu, X.; Pal, S.; Wang, S.; Ober, C. K.; Giannelis, E. P., Extreme ultraviolet resist materials for sub-7 nm patterning. *Chem. Soc. Rev.* **2017**, *46* (16), 4855-4866.
- 25. Jun, S.; Jang, E.; Park, J.; Kim, J., Photopatterned semiconductor nanocrystals and their electroluminescence from hybrid light-emitting devices. *Langmuir* **2006**, *22* (6), 2407-2410.
- 26. Wei, Y.; Li, X.; Chen, Y.; Cheng, Z.; Xiao, H.; Li, X.; Ding, J.; Lin, J., In Situ Light-Initiated Ligands Cross-Linking Enables Efficient All-Solution-Processed Perovskite Light-Emitting Diodes. *J. Phys. Chem. Lett.* **2020**, *11* (3), 1154-1161.
- 27. Hahm, D.; Park, J.; Jeong, I.; Rhee, S.; Lee, T.; Lee, C.; Chung, S.; Bae, W. K.; Lee, S., Surface Engineered Colloidal Quantum Dots for Complete Green Process. *ACS Appl. Mater. Interfaces* **2020**, *12* (9), 10563-10570.
- 28. Kim, W. J.; Kim, S. J.; Lee, K.-S.; Samoc, M.; Cartwright, A. N.; Prasad, P. N., Robust microstructures using UV photopatternable semiconductor nanocrystals. *Nano Lett.* **2008**, *8* (10), 3262-3265.
- 29. Zhu, J.; Lin, H.; Kim, Y.; Yang, M.; Skakuj, K.; Du, J. S.; Lee, B.; Schatz, G. C.; Van Duyne, R. P.; Mirkin, C. A., Light-Responsive Colloidal Crystals Engineered with DNA. *Adv. Mater.* **2020**, *32* (8), 1906600.
- 30. Wang, Y.; Fedin, I.; Zhang, H.; Talapin, D. V., Direct optical lithography of functional inorganic nanomaterials. *Science* **2017**, *357* (6349), 385-388.
- 31. Wang, Y.; Pan, J.-A.; Wu, H.; Talapin, D. V., Direct Wavelength-Selective Optical and Electron-Beam Lithography of Functional Inorganic Nanomaterials. *ACS Nano* **2019**, *13* (12), 13917-13931.

- 32. Talapin, D. V.; Lee, J.-S.; Kovalenko, M. V.; Shevchenko, E. V., Prospects of Colloidal Nanocrystals for Electronic and Optoelectronic Applications. *Chem. Rev.* **2010**, *110* (1), 389-458.
- 33. Dammel, R., Diazonaphthoquinone-based resists. SPIE press: 1993; Vol. 11.
- 34. Zhang, H.; Jang, J.; Liu, W.; Talapin, D. V., Colloidal nanocrystals with inorganic halide, pseudohalide, and halometallate ligands. *ACS Nano* **2014**, *8* (7), 7359-7369.
- 35. Dong, A.; Ye, X.; Chen, J.; Kang, Y.; Gordon, T.; Kikkawa, J. M.; Murray, C. B., A generalized ligand-exchange strategy enabling sequential surface functionalization of colloidal nanocrystals. *J. Am. Chem. Soc.* **2010**, *133* (4), 998-1006.
- 36. Nag, A.; Kovalenko, M. V.; Lee, J.-S.; Liu, W.; Spokoyny, B.; Talapin, D. V., Metal-free inorganic ligands for colloidal nanocrystals: S2-, HS-, Se2-, HSe-, Te2-, HTe-, TeS32-, OH-, and NH2-as surface ligands. *J. Am. Chem. Soc.* **2011**, *133* (27), 10612-10620.
- 37. Huang, J.; Liu, W.; Dolzhnikov, D. S.; Protesescu, L.; Kovalenko, M. V.; Koo, B.; Chattopadhyay, S.; Shenchenko, E. V.; Talapin, D. V., Surface functionalization of semiconductor and oxide nanocrystals with small inorganic oxoanions (PO43–, MoO42–) and polyoxometalate ligands. *ACS Nano* **2014**, *8* (9), 9388-9402.
- 38. Rodionova, G.; Yablokova, V.; Tuchin, Y. G.; Partalla, N.; Érlikh, R., Absorption spectra and structures of some o-naphthoquinone diazides. *J. Appl. Spectrosc.* **1989**, *51* (4), 1068-1071.
- 39. The ARChem SPARC Calculator. http://www.archemcalc.com/sparc-web/calc (accessed 3/2020).
- 40. Hilal, S. H.; Karickhoff, S. W.; Carreira, L. A., A Rigorous Test for SPARC's Chemical Reactivity Models: Estimation of More Than 4300 Ionization pKas. *Quant. Struct.-Act. Relat.* **1995,** *14* (4), 348-355.
- 41. Reiser, A.; Huang, J. P.; He, X.; Yeh, T. F.; Jha, S.; Shih, H. Y.; Kim, M. S.; Han, Y. K.; Yan, K., The molecular mechanism of novolak–diazonaphthoquinone resists. *Eur. Polym. J.* **2002**, *38* (4), 619-629.
- 42. Ellman, M.; Rodríguez, A.; Pérez, N.; Echeverria, M.; Verevkin, Y. K.; Peng, C. S.; Berthou, T.; Wang, Z.; Olaizola, S. M.; Ayerdi, I., High-power laser interference lithography process on photoresist: Effect of laser fluence and polarisation. *Appl. Surf. Sci.* **2009**, *255* (10), 5537-5541.
- 43. Khorasaninejad, M.; Capasso, F., Metalenses: Versatile multifunctional photonic components. *Science* **2017**, *358* (6367), eaam8100.
- 44. Prosser, J. H.; Brugarolas, T.; Lee, S.; Nolte, A. J.; Lee, D., Avoiding cracks in nanoparticle films. *Nano Lett.* **2012**, *12* (10), 5287-5291.
- 45. Lin, Q.; Yun, H. J.; Liu, W.; Song, H.-J.; Makarov, N. S.; Isaienko, O.; Nakotte, T.; Chen, G.; Luo, H.; Klimov, V. I., Phase-transfer ligand exchange of lead chalcogenide quantum dots for direct deposition of thick, highly conductive films. *J. Am. Chem. Soc.* **2017**, *139* (19), 6644-6653.
- 46. Hausmann, D. M.; Kim, E.; Becker, J.; Gordon, R. G., Atomic layer deposition of hafnium and zirconium oxides using metal amide precursors. *Chem. Mater.* **2002**, *14* (10), 4350-4358.
- 47. Kim, S. J.; Yoon, D. H.; Rim, Y. S.; Kim, H. J., Low-temperature solution-processed ZrO2 gate insulators for thin-film transistors using high-pressure annealing. *Electrochem. Solid-State Lett.* **2011**, 14 (11), E35-E37.
- 48. Magnusson, R.; Gaylord, T. K., Diffraction efficiencies of thin phase gratings with arbitrary grating shape. *J. Opt. Soc. Am.* **1978**, *68* (6), 806-809.
- 49. Kim, B. H.; Staller, C. M.; Cho, S. H.; Heo, S.; Garrison, C. E.; Kim, J.; Milliron, D. J., High Mobility in Nanocrystal-Based Transparent Conducting Oxide Thin Films. *ACS Nano* **2018**, *12* (4), 3200-3208.
- 50. Lee, J.; Lee, S.; Li, G.; Petruska, M. A.; Paine, D. C.; Sun, S., A facile solution-phase approach to transparent and conducting ITO nanocrystal assemblies. *J. Am. Chem. Soc.* **2012**, *134* (32), 13410-13414.

- 51. Staller, C. M.; Gibbs, S. L.; Saez Cabezas, C. A.; Milliron, D. J., Quantitative Analysis of Extinction Coefficients of Tin-Doped Indium Oxide Nanocrystal Ensembles. *Nano Lett.* **2019**, *19* (11), 8149-8154.
- 52. Agrawal, A.; Cho, S. H.; Zandi, O.; Ghosh, S.; Johns, R. W.; Milliron, D. J., Localized Surface Plasmon Resonance in Semiconductor Nanocrystals. *Chem. Rev.* **2018**, *118* (6), 3121-3207.
- 53. Chen, X.; Mao, S. S., Titanium Dioxide Nanomaterials: Synthesis, Properties, Modifications, and Applications. *Chem. Rev.* **2007**, *107* (7), 2891-2959.
- 54. Zhang, S.; Cao, S.; Zhang, T.; Lee, J. Y., Plasmonic Oxygen-Deficient TiO2-x Nanocrystals for Dual-Band Electrochromic Smart Windows with Efficient Energy Recycling. *Adv. Mater.* **2020**, 2004686.
- 55. Cook, K. T.; Tettey, K. E.; Bunch, R. M.; Lee, D.; Nolte, A. J., One-step index-tunable antireflection coatings from aggregated silica nanoparticles. *ACS Appl. Mater. Interfaces* **2012**, *4* (12), 6426-6431.
- 56. Wang, H.; Chen, H.; Ni, B.; Wang, K.; He, T.; Wu, Y.; Wang, X., Mesoporous ZrO2 Nanoframes for Biomass Upgrading. *ACS Appl. Mater. Interfaces* **2017**, *9* (32), 26897-26906.
- 57. Fu, L.; Xie, L.; Fu, W.; Hu, S.; Zhang, Z.-B.; Leifer, K.; Engqvist, H.; Xia, W., Ultra-strong translucent glass ceramic with nanocrystalline, biomimetic structure. *Nano Lett.* **2018**, *18* (11), 7146-7154.
- 58. Beall, G. H.; Duke, D. A., Transparent glass-ceramics. J. Mater. Sci. 1969, 4 (4), 340-352.
- 59. Hines, M. A.; Guyot-Sionnest, P., Synthesis and Characterization of Strongly Luminescing ZnS-Capped CdSe Nanocrystals. *The Journal of Physical Chemistry* **1996**, *100* (2), 468-471.
- 60. Yu, H.; Chen, M.; Rice, P. M.; Wang, S. X.; White, R. L.; Sun, S., Dumbbell-like Bifunctional Au–Fe₃O₄ Nanoparticles. *Nano Lett.* **2005**, *5* (2), 379-382.
- 61. Lounis, S. D.; Runnerstrom, E. L.; Bergerud, A.; Nordlund, D.; Milliron, D. J., Influence of dopant distribution on the plasmonic properties of indium tin oxide nanocrystals. *J. Am. Chem. Soc.* **2014**, 136 (19), 7110-7116.
- 62. Tirosh, E.; Markovich, G., Control of defects and magnetic properties in colloidal HfO₂ nanorods. *Adv. Mater.* **2007**, *19* (18), 2608-2612.